Inorganic Chemistry

pubs.acs.org/IC

Article

Tricarboxylic-Ligand-Decorated Lanthanoid-Inserted Heteropolyoxometalates Built by Mixed-Heteroatom-Directing Polyoxotungstate Units: Syntheses, Structures, and Electrochemical Sensing for 17β-Estradiol

Saisai Xie, Jun Jiang, Dan Wang,* Zhigang Tang, Runfei Mi, Lijuan Chen,* and Junwei Zhao*

Cite This: https://doi.org/10.1021/acs.inorgchem.1c00890

Read Online

ACCESS | Metrics & More | Article Recommendations | Supporting Information

ABSTRACT: Organic−inorganic hybrid metal−oxide clusters have been pursued for many years, benefiting from their abundant structures and prominent performances. Upon our exploration, a family of unusual mixed-heteroatom (Sb^{III}, P^{III})-directing lanthanoid (Ln)-inserted heteropolyoxotungstates (Ln-HPOTs), $[(CH_3)_2NH_2]_2Na_7H_3[Ln_4(HP^{III})W_8(H_2O)_{12}(H_2ptca)_2O_{28}]\cdot[Sb^{III}W_9O_{33}]_2\cdot 27H_2O$ [Ln = Ce^{3+} (**1**), La^{3+} (**2**), Pr^{3+} (**3**)], functionalized by 1,2,3-propanetricarboxylic acid (H_3ptca) was achieved. The intriguing trimeric $[Ln_4(HP^{III})W_8(H_2O)_{12}(H_2ptca)_2O_{28}][Sb^{III}W_9O_{33}]_2^{12-}$ polyanion was established by two trivacant $[B\text{-}\alpha\text{-}Sb^{III}W_9O_{33}]^{9-}$ segments mounted on both sides and one rare $[HP^{III}W_4O_{18}]^{8-}$ segment at the bottom, which are bridged via an organic−inorganic hybrid $[W_4Ln_4(H_2O)_{12}O_{10}(H_2ptca)_2]^{14+}$ central moiety. Such Ln-HPOTs involving dual-heteroatom-directing mixed building blocks, and even simultaneously modified by tricarboxylic ligands, are rather unseen in polyoxometalate chemistry. Moreover, the detection of 17β-estradiol through a **1**-based electrochemical biosensor has been explored, demonstrating a low detection limit (7.08×10^{-14} M) and considerable stability.

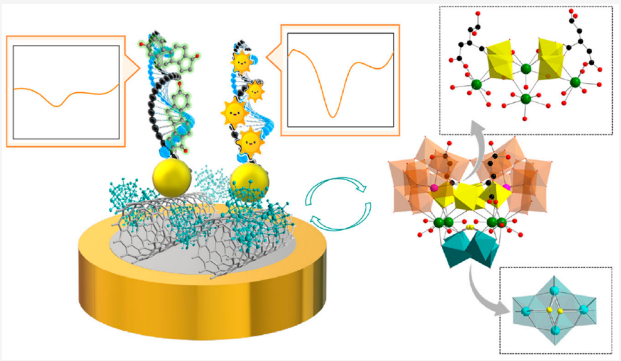

INTRODUCTION

Since the first heteropolyoxometalate (HPOM) $[PMo_{12}O_{40}]^{3-}$ was reported by Berzelius in 1826,[1] this enduring family has continued to greatly fascinate reseachers.[2−5] As the name suggests, HPOMs are a peculiar class of anionic metal−oxo clusters, which are normally fused by high-valence early-transition-metal−oxo $\{MO_m\}$ (M = V^V, Nb^V, Ta^V, Mo^{VI}, W^{VI}; m = 3−6) polyhedra and heteroatom−oxo $\{XO_m\}$ (m = 3, 4) polyhedra linked by sharing corners, edges, or faces.[6−10] Benefiting from their diverse structures and variable redox activities, HPOMs have demonstrated great potential as promising candidates in a wide range of applications in catalysis, medicine, and sensors.[11−18] A great number of studies have revealed that heteroatoms (HOAs, like Si^V, Ge^V, P^V, As^V, etc.), especially those with lone-pair electrons (e.g., As^{III}, Sb^{III}, Bi^{III}, etc.), present a remarkable stereochemistry-directing effect and can provide more chances to access lacunary HPOMs that possess high activities of being self-assembled into larger poly(HPOM) clusters or working as rigid polydentate ligands with strong nucleophilicity.[19−23] Therefore, implanting transition-metal (TM), lanthanide (Ln), or organic ligands into the HPOM system has been widely investigated to construct functional HPOM-based materials, most of which usually even display unexpected properties such as magnetism, optics, fluorescence, and proton conductivity.[24−28] As have been demonstrated by abundant researches, integrating Ln ions and HPOMs allows one to acquire more giant and fancy structures of poly(Ln-HPOM)s[29] for two important reasons: (i) variable coordination numbers and flexible coordination modes of Ln ions facilitate the bridging of HPOM fragments, resulting in fabulous poly(Ln-HPOM) structures; (ii) Ln contraction endows Ln ions with some essential discrepancies so that more diverse HPOM derivatives can be acquired. Therefore, pursuing novel Ln-HPOM aggregates has long been an attractive topic in polyoxometalate (POM) chemistry.[3,30]

Especially, the HOAs in group VA (M = P, As, Sb, Bi) have variable chemical valences (M^{III}/M^V) and disparate electronic configurations, which will potentially contribute to the

Received: March 23, 2021

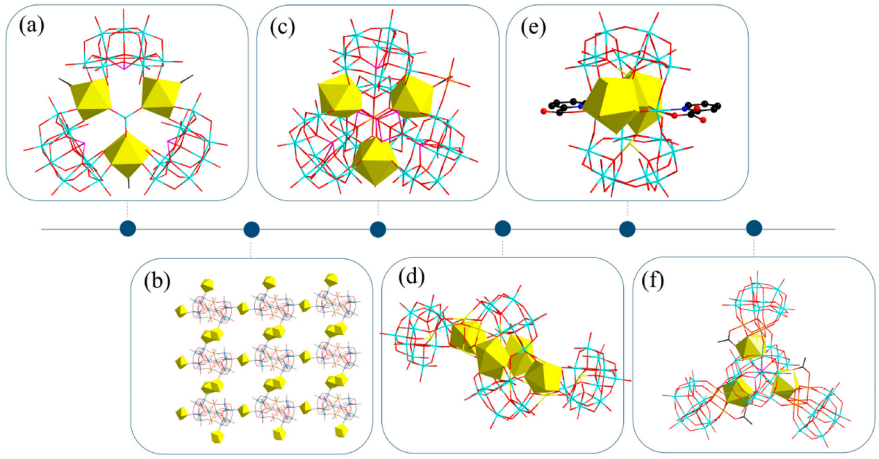

Figure 1. Structures of some Ln-SbWs: (a) **SbWCe$_3$**; (b) **SbWLn$_2$DOFe$_4$**; (c) **SbWLn$_3$Co$_2$**; (d) **SbWLn$_4$**; (e) **SbWLn$_2$**; (f) **SbPWLn$_3$Ni$_9$**. Color code: C, black; N, blue; O, red; {LnO$_x$} (x = 7, 8), bright yellow; {WO$_6$}, orange and aqua.

construction of more gorgeous HPOM structures. Hitherto, $P^{V/III}$, $As^{III/V}$, Sb^{III}, and Bi^{III} have been verified to be outstanding HOAs in the architecture of HPOMs. However, Sb^{V} and Bi^{V} show relatively strong hydrolysis and oxidicability in aqueous solution, which is why they are rarely used in related research. Moreover, although relevant studies about phosphotungstates and arsenotungstates have been comparatively sufficient, only some typical antimonotungstates (SbWs) have been reported. The acquirement of the first Eu^{3+}-substituted SbW $[Eu_3(H_2O)_3(SbW_9O_{33})(W_5O_{18})_3]^{18-}$ could be a landmark in the structural exploration of SbWs,[31] opening a fire-new research field of Ln-substituted SbWs (Ln-SbWs). In the following decades, some novel Ln-SbWs have been excavated in succession, such as $[(SbW_9O_{33})_4\{WO_2(H_2O)\}_2Ce_3(H_2O)_8(Sb_4O_4)]^{19-}$ (**SbWCe$_3$**; Figure 1a),[32] $[Ln(H_2O)_8]_2[Fe_4(H_2O)_8(thr)_2][B\text{-}\beta\text{-}SbW_9O_{33}]_2\cdot 22H_2O$ (**SbWLn$_2$Fe$_4$**; Ln = Pr^{3+}-Dy^{3+}, Lu^{3+} and thr = threonine; Figure 1b),[33] $[Pr(H_2O)_8][Pr(H_2O)_6][Fe_4(H_2O)_{10}(B\text{-}\beta\text{-}SbW_9O_{33})_2]\cdot 16H_2O$,[34] $[Sb_7W_{36}O_{133}Ln_3Co_2(OAc)(H_2O)_8]^{17-}$ (**SbWLn$_3$Co$_2$**; Ln = La^{3+}−Gd^{3+}; Figure 1c),[35] $\{[Ln_4(H_2O)_6Sb_6O_4](SbW_{10}O_{37})_2(SbW_8O_{31})_2\}^{22-}$ (**SbWLn$_4$**; Ln = Dy^{3+}-Er^{3+}, Y^{3+}; Figure 1d).[36] In all of the above-mentioned Ln-SbWs, Ln ions undoubtedly work as joints between SbW blocks, leading to larger clusters and even 2D networks. What is more, according to the hard and soft acid−base theory, Ln ions are electrophilic and can readily coordinate with N- or O-containing organic ligands. Thus, developing organic−inorganic hybrid Ln-SbWs has quickly become a hotspot in SbW chemistry. In 2011, an acetate-ornamented Y^{3+}-inserted trimer was prepared, in which acetate anions work as linkers between $[SbW_9O_{33}]^{9-}$ ({SbW_9}) moieties.[37] Subsequently, picolinic acid (Hpic) was introduced into the SbW system, providing a series of organic−inorganic hybrid Ln-SbWs $[Ln_2(H_2O)_4\{WO_2(pic)\}_2(SbW_8O_{30})_2]^{10-}$ (**SbWLn$_2$**; Ln = La^{3+}, Pr^{3+}; Figure 1e) and $[\{Ln(H_2O)\}\{Ln(pic)\}(Sb_3O_4)(SbW_8O_{31})(SbW_{10}O_{35})]_2^{24-}$ (Ln = Tb^{3+}−Ho^{3+}).[38] Although interest in SbWs has greatly increased, the continuous search for organic−inorganic hybrid Ln-SbWs is still in its infancy, which leaves much room for exploration.

A burgeoning theme in HPOM chemistry is preparing mixed-HOA-directing HPOMs. Typically, Kong et al. constructed two groundbreaking mixed-HOA-inserted HPOMs, $[Ln_3Ni_9(\mu_3\text{-}OH)_9(SbW_9O_{33})_2(P^VW_9O_{34})_3(CH_3COO)_3]^{30-}$ (**SbPWLn$_3$Ni$_9$**; Ln = Dy^{3+}, Er^{3+}; Figure 1f), simultaneously including two {SbW_9} fragments and a $[Ln_3Ni_9(\mu_3\text{-}OH)_9(P^VW_9O_{34})_3(CH_3COO)_3]$ cluster.[39] To our knowledge, investigation on mixed-HOA-inserted HPOMs remains underdeveloped hitherto, which provides us with a good opportunity for exploiting this field. As is known, although P^{III} with an intermediate valence might be highly active in forming lacunary phosphotungstate blocks, it has been much less studied compared with P^V. From the electron configuration, the trivalent phosphorus together with a proton can lead to a tetrahedral $[HP^{III}O_3]^{2-}$ geometry, which is somewhat distinctive from the lone-pair-electron-included $[Sb^{III}O_3]^{3-}$ trigonal-pyramidal templates. Therefore, it is believed that the synergistic effect of the tetrahedral $[HP^{III}O_3]^{2-}$ geometry and the $[Sb^{III}O_3]^{3-}$ trigonal-pyramidal geometry in the Ln-SbW system can construct novel multi-Ln-inserted mixed-HOA-directing HPOMs. This concept not only can enrich the structural diversity of multi-Ln-inserted HPOMs but also can stimulate cooperative research of the reaction ability of mixed HOAs in the system. Enlightened by such a particularity, we have devoted ourselves to synthesizing novel $[HP^{III}O_3]^{2-}$-inserted SbWs with some unexpected properties. As expected, we successfully obtained three (Sb^{III}, P^{III})-heteroatom-containing HPOMs decorated with H_3ptca, $[(CH_3)_2NH_2]_2Na_7H_3[Ln_4(HP^{III})W_8(H_2O)_{12}(H_2ptca)_2O_{28}][Sb^{III}W_9O_{33}]_2\cdot 27H_2O$ [Ln = Ce^{3+} (**1**), La^{3+} (**2**), Pr^{3+} (**3**)]. It is noteworthy that the organic−inorganic hybrid $[Ln_4(HP^{III})W_8(H_2O)_{12}(H_2ptca)_2O_{28}][Sb^{III}W_9O_{33}]_2^{12-}$ polyanion (PA) especially holds two Keggin-type {SbW_9} subunits as well as one unprecedented $[HP^{III}W_4O_{20}]^{12-}$ ({$HP^{III}W_4$}) moiety. More interestingly, the H_2ptca^- ligand was formed through an in situ reaction of itaconic acid and carbon dioxide from air.[40−42] So far, HPOMs, especially those composited with guest materials [e.g., metal nanoparticles, carbon nanotubes (CNs), graphene], have made great progress in electrochemical (EC) biosensors. Consequently, because of its outstanding redox activity of HPOMs and promising potential in electrochemistry,[43] **1** has been composited with a carboxyl-functionalized multiwalled carbon nanotube (CFMCN), and the resulting composite has further functioned as a valuable candidate in EC-sensing 17β-estradiol (EDO), which shows good sensing selectivity, a low limit of detection (LOD = 7.08×10^{-14} M), and good stability.

https://doi.org/10.1021/acs.inorgchem.1c00890
Inorg. Chem. XXXX, XXX, XXX−XXX

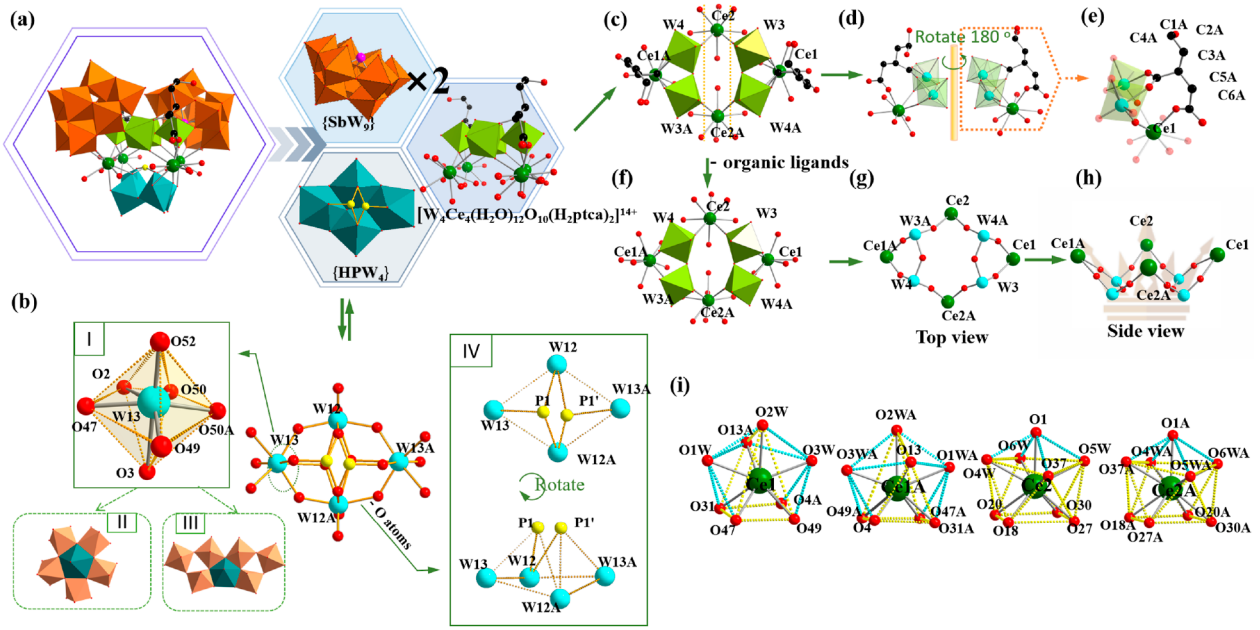

Figure 2. (a) Trimeric **1a**. (b) $[HP^{III}W_4O_{18}]^{8-}$ moiety (inset I, decanedron configuration of a seven-coordinate W atom; insets II and III, seven-coordinate W configurations in the reported works; inset IV, simplified graph of the P^{III} center and four main W atoms). (c) Ce^{3+} ions in **1b**. (d) C_2 symmetry in **1b**. (e) Chelating H_2ptca^- ligand in **1c**. (f) Pure inorganic $[W_4Ce_4(H_2O)_{12}O_{10}]^{16+}$. (g) Top view of the $\{W_4Ce_4\}$ skeleton. (h) Side view of the crownlike $\{W_4Ce_4\}$ skeleton. (i) Bicapped trigonal-prismatic geometry of $Ce1^{3+}$ and $Ce1A^{3+}$ ions and monocapped square-antiprismatic configuration of $Ce2^{3+}$ and $Ce2A^{3+}$ ions. Symmetry code: A, $1 - x, y, 1.5 - z$.

RESULTS AND DISCUSSION

Structure Description. **1**–**3** possess the same crystal structure in the *C*2/*c* space group (Table S1), as evidenced by IR spectra (Figure S1) and powder X-ray diffraction (PXRD; Figure S2). Furthermore, using thermogravimetric analysis (TG; Figure S3), elemental analysis, and inductively coupled plasma atomic emission spectrometry, their molecular formulas are identified as $[(CH_3)_2NH_2]_2Na_7H_3[Ln_4(HP^{III})W_8(H_2O)_{12}(H_2ptca)_2O_{28}][Sb^{III}W_9O_{33}]_2{\cdot}27H_2O$ [Ln = Ce^{3+} (**1**), La^{3+} (**2**), Pr^{3+} (**3**)], giving a H_2ptca^--modified trimeric $[Ln_4(HP^{III})W_8(H_2O)_{12}(H_2PTCA)_2O_{28}][Sb^{III}W_9O_{33}]_2^{12-}$ PA. The crystal structure of **1** will be elaborated on for a deep understanding of the skeleton. The $[Ce_4(HP^{III})W_8(H_2O)_{12}(H_2PTCA)_2O_{28}][Sb^{III}W_9O_{33}]_2^{12-}$ (**1a**) PA is an unprecedented trimeric Ce^{3+}-substituted MHOAIHPOM cluster decorated with two H_2ptca^- ligands (Figure 2a). For more details, **1a** can be divided into two trivacant Keggin-type $\{SbW_9\}$ segments mounted on both sides and one $\{HPW_4\}$ fragment located at the bottom, which are bridged by an organic–inorganic hybrid $[W_4Ce_4(H_2O)_{12}O_{10}(H_2ptca)_2]^{14+}$ (**1b**) central linker. Different from a traditional six-coordinate $\{WO_6\}$ octahedron, four W atoms in the $\{HPW_4\}$ part show an uncommon seven-coordinate $\{WO_7\}$ decahedron configuration (Figure 2b, inset I) and are connected by sharing O bridges. As is known, such seven-coordinate W atoms have been seen in a $\{WV_5\}$ core containing a $\{V_5\}$ ring connected with a central $\{WO_7\}$ in an edge-sharing pattern (Figure 2b, inset II)[44] as well as a particular $\{W_7\}$ building block including a central $\{WO_7\}$ and six $\{WO_6\}$ (Figure 2b, inset III).[45] Besides, the P^{III} center and four W atoms present a quadrangular pyramid arrangement with P^{III} located at the vertex (Figure 2b, inset IV). Furthermore, a detailed explanation of **1b** is critically necessary for a better understanding of the whole crystal structure. While some O atoms shared with the $\{SbW_9\}$ unit are also considered, this cluster can be viewed as two $[W_2Ce(H_2O)_3O_3(H_2ptca)]^{8+}$ (**1c**) segments connected by two Ce^{3+} ions (Figure 2c) and interestingly displays C_2 symmetry (Figure 2d). After removal of two bridging $Ce2^{3+}$ ions ($Ce2^{3+}$ and $Ce2A^{3+}$) in either **1c** cluster, the remaining one $Ce1^{3+}$ ion and two W atoms from the $\{W_2O_{11}\}$ subunit share two μ_2-O atoms. In the meantime, the $Ce1^{3+}$ ion and $\{W_2O_{11}\}$ subunit are joined by a H_2ptca^- ligand via carboxyl O atoms (Figure 2e). The interesting thing is that, even if organic ligands are ignored, the overall skeleton of the $\{W_4Ce_4\}$ fragment is still retained, with $\{WO_6\}$ moieties serving as the linkers (Figure 2f). What is more, the W atoms and Ce^{3+} ions make up a jagged polygon, while nonbridging O atoms are removed, which can be viewed as a regular rhombus from the top view (Figure 2g) or a crownlike configuration from the side view (Figure 2h). Therein, four Ce^{3+} ions demonstrate two different types of coordination modes. Specifically, the eight-coordinate $Ce1^{3+}$ and $Ce1A^{3+}$ present a bicapped trigonal-prismatic geometry, while two nine-coordinate $Ce2^{3+}$ and $Ce2A^{3+}$ ions exhibit a distorted monocapped square-antiprismatic geometry (Figure 2i). Looking further into the connection between different W–O clusters, the two $\{SbW_9\}$ moieties are connected by double W–O–W bridges by sharing apical O atoms (Figure 3a). Moreover, each $\{SbW_9\}$ part is attached to the $\{HPW_4\}$ fragment via a Ce^{3+} ion (Figure 3b), while four Ce^{3+} ions further act as inorganic linkers clawing the $\{HPW_4\}$ cluster and two central $\{W_2O_{11}\}$ clusters (Figure 3c).

By the assistance of the countercations ($[H_2N(CH_3)_2]^+$, Na^+, and H^+, **1a** PAs stack into an ordered supramolecular 3D structure (Figure S4). As viewed from the *a* direction, adjacent **1a** PAs are arranged in the –ABAB– mode along the *c* axis, while adjacent **1a** PAs along the *b* axis are aligned in the –AAA– mode (Figure S4a,b). Analogously, as viewed from the *b* direction, neighboring **1a** PAs stand in the –ABAB–

https://doi.org/10.1021/acs.inorgchem.1c00890
Inorg. Chem. XXXX, XXX, XXX–XXX

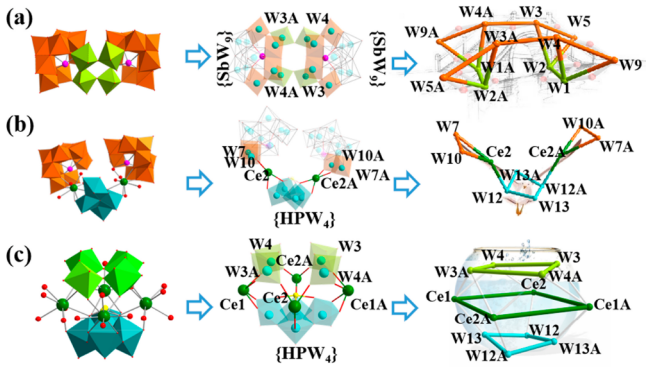

Figure 3. (a) View of two $\{SbW_9\}$ fragments bridged by two $\{W_2O_{11}\}$ groups. (b) Connection between $\{HPW_4\}$ and two $\{SbW_9\}$ moieties. (c) Combination of Ce^{3+} ions and a $\{HPW_4\}$ fragment. Symmetry code: A, $1 - x, y, 1.5 - z$.

mode along the *a* or *c* axis (Figure S4c,d). When the gaze shifts to the *c* direction, neighboring **1a** PAs are also arranged in the −ABAB− mode along the *a* or *b* axis (Figure S4e,f).

Construction of a 1-Based EC Biosensor (ECB). As one of the most active estrogens, EDO plays a critical role in the human body, which not only promotes and maintains the physiological action of the secondary sexual characteristics but also has obvious effects on endocrine, cardiovascular, metabolic system, bone growth and maturity, skin, and some other physiological activities.[46] An abnormal EDO level can undoubtedly break the physiological balance and further affect human health, which makes a sensitive EDO biosensor an urgent issue. To date, there have been some eye-catching reports on HPOM-based biosensors for the sensitive detection of acetaminophen, ascorbic acid, and uric acid.[47−49]

Developing HPOM-based materials in EC-sensing and biosensor applications has been acknowledged as one of the most promising potentials in POM chemistry, owing to the ideal reversible charge-transfer capability of HPOMs.[50−53] Studies have demonstrated that HPOMs can act as efficient electron donors or acceptors without structural change, which makes HPOMs valuable candidates for electron-exchange reactions. Because of their unique electronic structure, CNs have been favorably investigated to prepare POM−CN composites, in which a combination of POMs and CNs will contribute to a significantly enhanced electronic transport capability.[54] Considering all of the above-mentioned factors, the composite of **1** with CFMCN has been proposed to modify glassy carbon electrodes (GCEDs) for further the EC detection of EDO. The preparation and sensing processes of **1**-based ECBs are graphically represented in Schemes 1 and 2, respectively. As illustrated, the **1**@CFMCN composite (Scheme 1a−c) is dropped on the surface of a GCED (Scheme 1d) with Nafion as the binder to manufacture a **1**@CFMCN-modified GCED (**1**@CFMCN-GCED; Scheme 1e), followed by the EC deposition process of gold nanoparticles (Au NPs) on the surface constructing Au/**1**@CFMCN-GCED (Scheme 1f). After the aptamer (apta) of EDO is grafted onto Au/**1**@CFMCN-GCED via Au−S bonds, the remaining naked Au sites are covered by 6-mercapto-1-hexanol (MHN), generating apta/Au/**1**@CFMCN-GCED (Schemes 1g and 2a).

In the EC detection process, if we use apta/Au/**1**@CFMCN-GCED to directly detect EDO, although apta specifically captures EDO (Scheme 2a,b), the change of the EC responsive signal for apta/Au/**1**@CFMCN-GCED cannot be read out, which leads to a failure to detect EDO. However, because cDNA can competitively bind with apta (compared with EDO), we can detect cDNA by using apta/Au/**1**@CFMCN-GCED and further realize the detection of EDO because the amount of cDNA on apta/Au/**1**@CFMCN-GCED is inversely proportional to the amount of EDO on apta/Au/**1**@CFMCN-GCED. That is, for a given apta/Au/**1**@CFMCN-GCED, the more apta is combined with cDNA, the less apta is combined with EDO. It is known that cDNA on cDNA/apta/Au/**1**@CFMCN-GCED (Scheme 2c) can bind methylene blue (MB; Scheme 2d), resulting in a noticeable change of the read-out EC responsive signal for cDNA/apta/Au/**1**@CFMCN-GCED, which has been experimentally testified.[55] Apparently, because of the preferred combination

Scheme 1. Schematic Preparation Process of 1@CFMCN-GCED

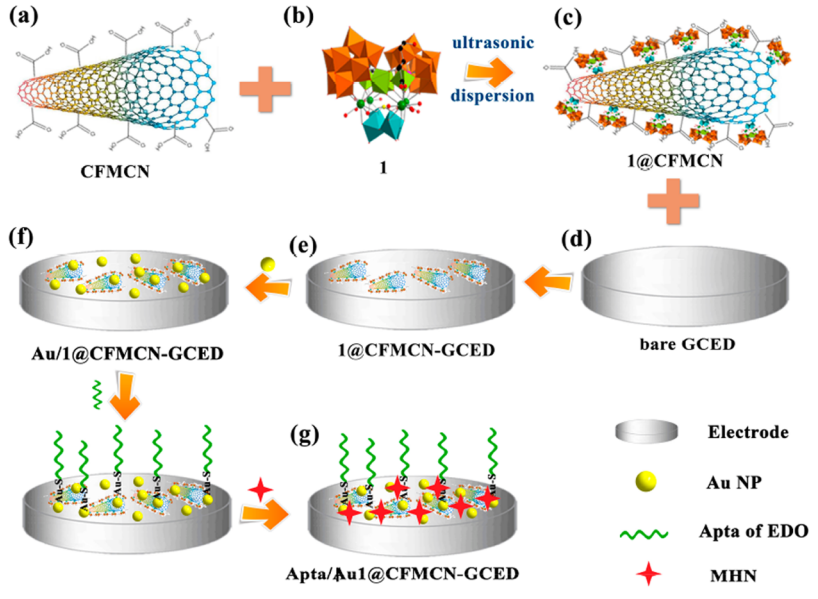

https://doi.org/10.1021/acs.inorgchem.1c00890
Inorg. Chem. XXXX, XXX, XXX−XXX

Scheme 2. Construction and Illustration of the Strategy for Detecting EDO Based on cDNA/apta/Au/1@CFMCN-GCED

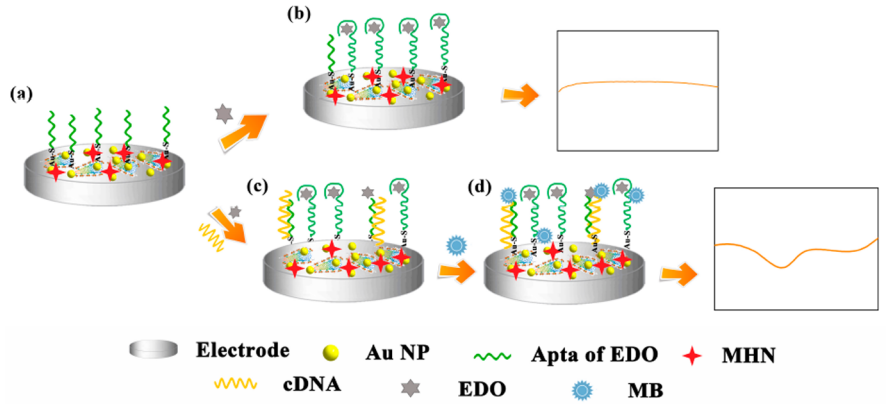

effect of EDO (compared with cDNA) and apta, the read-out EC responsive signal intensity for cDNA/apta/Au/**1**@CFMCN-GCED is inversely proportional to the amount of EDO. Here, MB plays a signal-indicator role in the process of detecting EDO.

Specifically, the uniformly dispersed **1**@CFMCN composite has been clearly demonstrated by scanning electron microscopy (SEM; Figure 4a) and transmission electron microscopy (TEM; Figure 4b). Furthermore, the high-angle annular-dark-field scanning transmission electron microscopy (HAADF-STEM) image (Figure 4c) and STEM−energy-dispersive spectroscopy (EDS) elemental mapping graph (Figures 4d and S5) show the well distribution of P, Sb, Ce, and W elements, which indicates the successful adhesion of **1** and CFMCN. Moreover, IR and Raman spectra show that the **1**@CFMCN composite undoubtedly contains the characteristic peaks of **1** and CFMCN, identifying not only the successful complexation of **1** and CFMCN but also the structure maintenance of **1** (Figure S6). After that, Au NPs are electrochemically deposited on **1**@CFMCN-GCED, while the morphology and Au NPs are characterized by SEM (Figure 4e) and EDS (Figure 4f). Considering better resolution and higher current sensitivity compared with cyclic voltammetry (CV), differential pulse voltammetry (DPV) is a more sensitive method to explore the EC performances.[56] Therefore, the EC performances of **1**-based ECBs were mainly studied by the DPV tests.

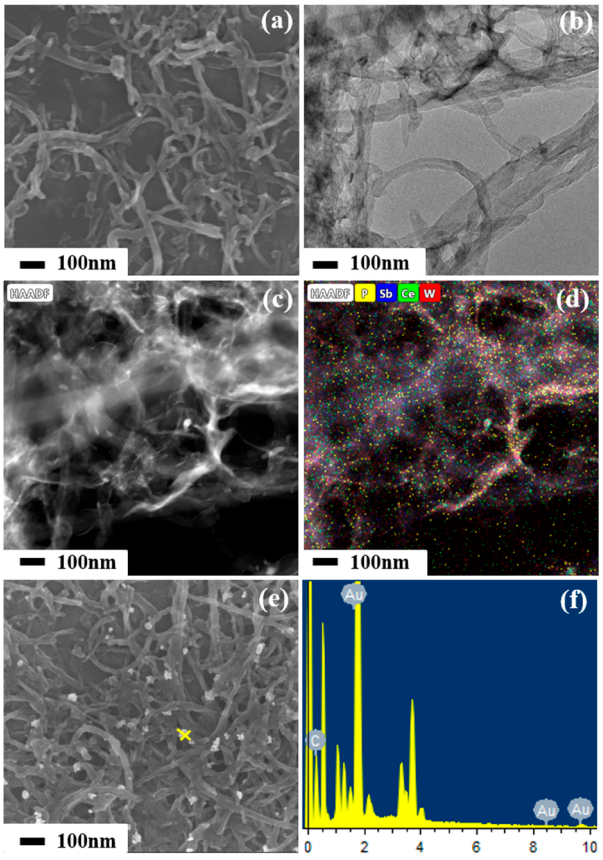

Figure 4. (a) SEM, (b) TEM, (c) HAADF-STEM, and (d) STEM-EDS elemental mapping images of the **1**@CFMCN composite on the indium−tin oxide (ITO) conductive glass. (e) SEM and (f) EDS images of Au-deposited the **1**@CFMCN composite on the ITO conductive glass.

EC Performances of 1-Based ECBs. First of all, some key parameters for **1**@CFMCN-GCED working as the EDO identification platform, which will affect EC-sensing performances, were optimized. (1) Determination of the proper electrodeposition time (EDT) of Au NPs on **1**@CFMCN-GCED. Because Au NPs can significantly improve the conductivity of the modified GCED, Au/**1**@CFMCN-GCEDs prepared under various EDTs (20/40/60/70/80/90/100/120 s) were evaluated by DPV (Figure 5a) methods in 1.00 mM $[Fe(CN)_6]^{3-/4-}$ in order to obtain good conductivity. As can be obviously observed from the trend of the DPV peak current intensity (Figure 5b), the conductivity of Au/**1**@CFMCN-GCEDs grows up with increasing EDT from 20 to 80 s, but longer EDT (>80 s) results in worse conductivity, for which it can be supposed that longer EDT generates the agglomeration of larger Au particles on the surface of **1**@CFMCN-GCEDs, leading to less available Au sites. As a result, 80 s is selected as the favorable EDT for the subsequent measurement. (2) Optimization of the proper concentration of apta for EDO grafting on Au/**1**@CFMCN-GCE. The appropriate apta concentration is the guarantee of the sufficient capture of EDO. As depicted in Figure 5c,d, the DPV peak current of Au/**1**@CFMCN-GCED decreases after being treated with an apta solution overnight with increasing apta concentration. When the apta concentration is up to 0.10 μM, the graft of apta on the surface of Au/**1**@CFMCN-GCED gradually reaches saturation, and the DPV peak current of Au/**1**@CFMCN-GCED remains almost unchanged. Therefore, 0.1 μM apta was employed in the following experiments for

https://doi.org/10.1021/acs.inorgchem.1c00890
Inorg. Chem. XXXX, XXX, XXX−XXX

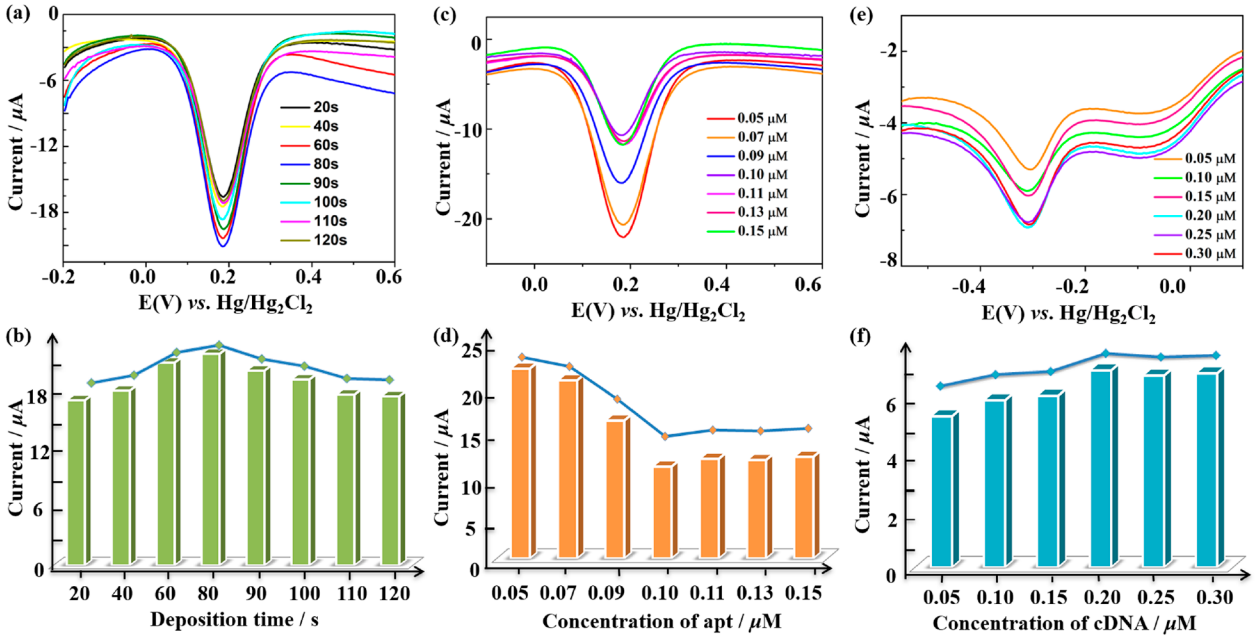

Figure 5. (a) DPV curves of Au/**1**@CFMCN-GCEDs prepared under different EDTs. (b) Dependence of the DPV peak current of Au/**1**@CFMCN-GCEDs with EDTs. (c) DPV curves of Au/**1**@CFMCN-GCED in different apta concentrations. (d) Dependence of the DPV peak current of Au/**1**@CFMCN-GCED with apta concentrations. (e) DPV curves of apta/Au/**1**@CFMCN-GCED in different cDNA concentrations. (f) Dependence of the DPV peak current of apta/Au/**1**@CFMCN-GCED with cDNA concentrations.

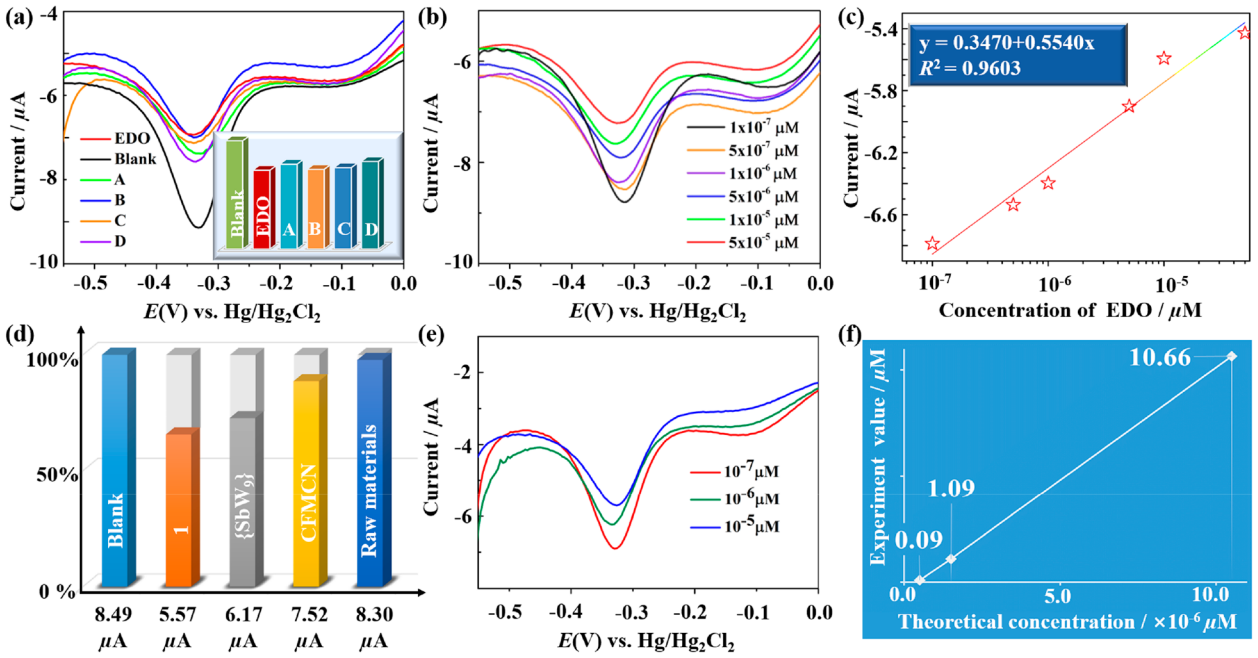

Figure 6. (a) DPV curves and current intensities (insert) of **1**-based ECBs detecting different mixed targets. (b) Variation of the DPV curves with different concentrations of EDO. (c) Linear fitting of the plot of the DPV current intensity and concentration of EDO. (d) EC detection performance of different GCEs modified by different materials [raw materials: $NaWO_4{\cdot}2H_2O$ + H_3PO_3 + H_3ptca + $Ce(AC)_3$]. The EC signal of 8.49 μA read from the contrast test is viewed as 100%. (e and f) EC detection of (10^{-5}, 10^{-6}, and 10^{-7} μM) in serum.

competitive binding with EDO. (3) Determination of the proper cDNA concentration on apta/Au/ **1**@CFMCN-GCED. The effect of the cDNA concentration on apta/Au/**1**@CFMCN-GCED was also examined in the cDNA concentration range of 0.05−0.30 μM via the DPV method in a 50.0 mM Tris-HCl solution. As shown in Figure 5e,f, the signal of MB first increases with an increase of the concentration of cDNA. When the concentration of cDNA reaches 0.2 μM, the signal of MB begins to stabilize. Therefore, the optimal cDNA concentration is 0.20 μM because no distinct current augment appears while the cDNA concentration further grows, hinting at saturation of cDNA capture. The **1**-based ECB prepared under optimal conditions is named cDNA/apta/Au/**1**@CFMCN-GCED. In addition, in order to identify that **1** can enhance the EC properties in the modified electrodes, CV curves of the GCED electrodes modified by different materials

https://doi.org/10.1021/acs.inorgchem.1c00890
Inorg. Chem. XXXX, XXX, XXX−XXX

such as **1**@CFMCN-GCED, Au/**1**@CFMCN-GCED, apta/Au/**1**@ CFMCN-GCED, and cDNA/apta/Au/**1**@CFMCN-GCED have been measured (Figure S7). Experimental results demonstrate that the conductivity of all of the modified electrodes is better than that of the bare GCE, which further indicates that **1** indeed plays an important role in improving the EC properties of modified electrodes.

Under optimal conditions, the EC performances of cDNA/apta/Au/**1**@CFMCN-GCED for detecting EDO were evaluated. First of all, **1**−**3** were all applied to construct the EDO biosensor, so that the possible influence of different RE ions (La^{3+}, Ce^{3+}, or Pr^{3+}) was excluded because they showed almost the same signals (Figure S8). In this work, we selected the Ce^{3+}-inserted **1** to complete the performance evaluation of the EC sensor. To examine the antiinterference performance, as an important evaluation index for the subsequent study of cDNA/apta/Au/**1**@CFMCN-GCED for sensing EDO, the DPV tests of a series of solutions containing EDO and bisphenol A (A, 8 μL), EDO and cholesterol (B, 8 μL), EDO and 1-aminoanthraquinone (C, 8 μL), or all four biomolecules (D, each of these is equal to 8 μL) were carried out in a 50.0 mM Tris-HCl solution (the concentration of each target is 10^{-5} μM; Figure 6a). As shown in Figure 6a, no significant influence on the DPV signal can be observed, while other biomolecules coexist with EDO. This may be due to the specific binding ability of apta to EDO. Hence, this consequence expressly demonstrated that the as-prepared sensor is free from interferences of these biomolecules. Subsequently, a series of EC tests of cDNA/apta/Au/**1**@CFMCN-GCED recognizing EDO in different concentrations were studied. As the concentration of EDO increases, the number of cDNA bound to cDNA/apta/Au/**1**@CFMCN-GCED will reduce, which causes a decrease of the number of MB grafting to cDNA/apta/Au/**1**@CFMCN-GCED; thus, the EC signal of MB will decline. As expected, the higher the concentration of EDO, the weaker the EC signal of MB (Figure 6b). What is more, the EC signal strength presents a good linear relationship, while the concentration of EDO ranges from 1.0×10^{-7} to 5.0×10^{-5} μM ($y = 0.5540x + 0.3470$, and the linear correlation $R^2 = 0.960$; Figure 6c). Thus, a LOD is calculated as 7.08×10^{-8} μM on the base of 5 times the standard blank sample measured deviation. Compared with some previously reported work on the EC detection of EDO (Table S2), a **1**-based ECB shows a lower LOD of EDO detection, indicating the great potential and utility of POMs in ECBs. As another indispensable index in potentially practical applications, the stability of **1**-based ECBs was also explored by keeping the modified electrode (**1**@CFMCN-GCED) at room temperature for 6 days. Furthermore, a EDO (10^{-5} μM) detection test was carried out using the stored electrodes, and the obtained results indicate that the DPV curves of **1**-based ECBs remain almost unchanged for 6 days, verifying the good stability for EC application (Figure S9a).

To further evaluate the importance of **1** in cDNA/apta/Au/**1**@CFMCN-GCED for sensing EDO, the mixture of raw materials [$NaWO_4 \cdot 2H_2O$, H_3PO_3, H_3ptca, and $Ce(AC)_3$] composited with CFMCNs, the pure {SbW_9} precursor composited with CFMCNs, and the pure CFMCNs have been respectively applied to modify the GCEDs under the same conditions for EDO detection (the concentration of EDO is 10^{-5} μM). Beyond all doubt, it turns out that the **1**-based ECBs (orange column) perform better than any other tested materials (Figures 6d and S9b). This may be because Ce^{3+} ions are positively charged and CFMCN may undergo deionization in aqueous solution. Through electrostatic interaction, the CFMCNs combine with Ce^{3+} ions, which is not conducive to the dispersion of CFMCNs. Although $NaWO_4 \cdot 2H_2O$ or {SbW_9} can promote the dispersion of CFMCNs in aqueous solution, the volume of WO_4^{2-} or {SbW_9} is relatively small compared to this anion cluster, so it is not effective in promoting dispersion compared to this large anion cluster. Therefore, if the CFMCNs are well dispersed, the surface of the electrode is more uniform, and the monitoring effect of EDO will be better. The EDO detection results of these modified electrodes are intimately related to their conductivity, which results from the composition of the modified electrode (Figure S10). To estimate the application potential of the **1**-based ECB, 1000-fold diluted human serum solutions containing different concentrations of EDO (10^{-5}, 10^{-6}, and 10^{-7} μM) were measured by the DPV technique (Figure 6e,f). Excitingly, the **1**-based ECB works efficaciously in detecting EDO in the serum solution because the experimental values are very close to the theoretical values as the deviations (10^{-5} μM, 6.6%; 10^{-6} μM, 9.0%; 10^{-7} μM, 10.0%) are acceptable. The results show that the proposed sensor offered a reliable and accurate method to monitor EDO. As a result, all of the experimental results can make it believable that a **1**-based ECB can be a promising candidate for EDO determination.

CONCLUSIONS

In summary, the first mixed-heteroatom (Sb^{III}, P^{III})-directing HPOMs **1**−**3** have been obtained and structurally characterized. It is noteworthy that the fascinating mixed-HOA-inserted $[Ln_4(HP^{III})W_8(H_2O)_{12}(H_2ptca)_2O_{28}]$-$[Sb^{III}W_9O_{33}]_2^{12-}$ trimeric PA in **1**−**3** is constructed from two trilacunary $[B\text{-}\alpha\text{-}Sb^{III}W_9O_{33}]^{9-}$ segments and one rare $[HP^{III}W_4O_{18}]^{8-}$ segment, which are bridged via an organic−inorganic hybrid $[W_4Ln_4(H_2O)_{12}O_{10}(H_2ptca)_2]^{14+}$ central moiety. Furthermore, **1** has been composited with CFMCN and further explored as a valuable candidate in EC-sensing EDO, which shows considerable sensitivity and stability. Therefore, this work not only provides valuable ideas of introducing mixed HOAs along with organic ligands into the POM system to construct novel mixed-HOA-directing HPOMs but also broadens the application of HPOM-based composite materials in bioanalysis, and even more importantly clinical medicine.

ASSOCIATED CONTENT

Supporting Information

The Supporting Information is available free of charge at https://pubs.acs.org/doi/10.1021/acs.inorgchem.1c00890.

PXRD patterns, IR spectra, TG curves, SEM and TEM images, EDS graphs, CV and DPV curves, and related schematic presentation (PDF)

Accession Codes

CCDC 2062494−2062496 contain the supplementary crystallographic data for this paper. These data can be obtained free of charge via www.ccdc.cam.ac.uk/data_request/cif, or by emailing data_request@ccdc.cam.ac.uk, or by contacting The Cambridge Crystallographic Data Centre, 12 Union Road, Cambridge CB2 1EZ, UK; fax: +44 1223 336033.

https://doi.org/10.1021/acs.inorgchem.1c00890
Inorg. Chem. XXXX, XXX, XXX−XXX

AUTHOR INFORMATION

Corresponding Authors

Dan Wang − *Henan Key Laboratory of Polyoxometalate Chemistry, College of Chemistry and Chemical Engineering, Henan University, Kaifeng, Henan 475004, China*; Email: wangdan@henu.edu.cn

Lijuan Chen − *Henan Key Laboratory of Polyoxometalate Chemistry, College of Chemistry and Chemical Engineering, Henan University, Kaifeng, Henan 475004, China*; Email: ljchen@henu.edu.cn

Junwei Zhao − *Henan Key Laboratory of Polyoxometalate Chemistry, College of Chemistry and Chemical Engineering, Henan University, Kaifeng, Henan 475004, China*; orcid.org/0000-0002-7685-1309; Email: zhaojunwei@henu.edu.cn

Authors

Saisai Xie − *Henan Key Laboratory of Polyoxometalate Chemistry, College of Chemistry and Chemical Engineering, Henan University, Kaifeng, Henan 475004, China*

Jun Jiang − *Henan Key Laboratory of Polyoxometalate Chemistry, College of Chemistry and Chemical Engineering, Henan University, Kaifeng, Henan 475004, China*

Zhigang Tang − *Henan Key Laboratory of Polyoxometalate Chemistry, College of Chemistry and Chemical Engineering, Henan University, Kaifeng, Henan 475004, China*

Runfei Mi − *Henan Key Laboratory of Polyoxometalate Chemistry, College of Chemistry and Chemical Engineering, Henan University, Kaifeng, Henan 475004, China*

Complete contact information is available at: https://pubs.acs.org/10.1021/acs.inorgchem.1c00890

Notes

The authors declare no competing financial interest.

ACKNOWLEDGMENTS

This work was supported by the National Natural Science Foundation of China (Grants 21871077, 21671054, 21771052, and 22001042), the Program for Innovation Teams in Science and Technology in Universities of Henan Province (Grant 20IRTSTHN004), and the Program of First-Class Discipline Cultivation Project of Henan University (Grants 2019YLZDYJ02 and CJ1205A0240019).

REFERENCES

(1) Berzelius, J. J. Beitrag zur näheren kenntniss des molybdans. *Ann. Phys.* **1826**, *82*, 369−392.

(2) Coronado, E.; Gómez-García, C. J. Polyoxometalate-based molecular materials. *Chem. Rev.* **1998**, *98*, 273−296.

(3) Liu, J. C.; Han, Q.; Chen, L. J.; Zhao, J. W.; Streb, C.; Song, Y. F. Aggregation of giant cerium-bismuth tungstate clusters into a 3D porous framework with high proton conductivity. *Angew. Chem., Int. Ed.* **2018**, *57*, 8416−8420.

(4) Wang, S.-S.; Yang, G.-Y. Recent advances in polyoxometalate-catalyzed reactions. *Chem. Rev.* **2015**, *115*, 4893−4962.

(5) Boskovic, C. Rare earth polyoxometalates. *Acc. Chem. Res.* **2017**, *50*, 2205−2214.

(6) Liu, J. X.; Zhang, X. B.; Li, Y. L.; Huang, S. L.; Yang, G. Y. Polyoxometalate functionalized architectures. *Coord. Chem. Rev.* **2020**, *414*, 213260.

(7) Das, V.; Kaushik, R.; Hussain, F. Heterometallic 3d-4f polyoxometalates: An emerging field with structural diversity to multiple applications. *Coord. Chem. Rev.* **2020**, *413*, 213271.

(8) Fang, W. H.; Zhang, L.; Zhang, J. Synthetic strategies, diverse structures and tuneable properties of polyoxo-titanium clusters. *Chem. Soc. Rev.* **2018**, *47*, 404−421.

(9) Gao, M. Y.; Zhang, L.; Zhang, J. Preparation and properties of polyoxo-titanium clusters. *Kexue Tongbao* **2018**, *63*, 2731−2744.

(10) Marrot, J.; Pilette, M. A.; Haouas, M.; Floquet, S.; Taulelle, F.; López, X.; Poblet, J. M.; Cadot, E. Polyoxometalates paneling through $\{Mo_2O_2S_2\}$ coordination: cation-directed conformations and chemistry of a supramolecular hexameric scaffold. *J. Am. Chem. Soc.* **2012**, *134*, 1724−1737.

(11) Luo, W. J.; Hu, j.; Diao, H. L.; Schwarz, B.; Streb, C.; Song, Y. F. Robust polyoxometalate/nickel foam composite electrodes for sustained electrochemical oxygen evolution at high pH. *Angew. Chem., Int. Ed.* **2017**, *56*, 4941−4944.

(12) Fernandes, D. M.; Araújo, M. P.; Haider, A.; Mougharbel, A. S.; Fernandes, A. J. S.; Kortz, U.; Freire, C. Polyoxometalate-graphene electrocatalysts for the hydrogen evolution reaction. *ChemElectroChem* **2018**, *5*, 273−283.

(13) Liu, R. J.; Li, S. W.; Yu, X. L.; Zhang, G. J.; Ma, Y.; Yao, J. N. Facile synthesis of a Ag nanoparticle/polyoxometalate/carbon nanotube tri-component hybrid and its activity in the electrocatalysis of oxygen reduction. *J. Mater. Chem.* **2011**, *21*, 14917−14924.

(14) Li, H. L.; Liu, Y. J.; Liu, J. L.; Chen, L. J.; Zhao, J. W.; Yang, G. Y. Structural transformation from dimerization to tetramerization of serine-decorated rare-earth incorporated arsenotungstates induced by the usage of rare-earth salts. *Chem. - Eur. J.* **2017**, *23*, 2673−2689.

(15) Guo, S. X.; Li, F. W.; Chen, L.; MacFarlane, D. R.; Zhang, J. Polyoxometalate-promoted electrocatalytic CO_2 reduction at nanostructured silver in dimethylformamide. *ACS Appl. Mater. Interfaces* **2018**, *10*, 12690−12697.

(16) Bijelic, A.; Aureliano, M.; Rompel, A. Polyoxometalates as potential next-generation metallodrugs in the combat against cancer. *Angew. Chem., Int. Ed.* **2019**, *58*, 2980−2999.

(17) Wang, D.; Li, Y. M.; Zhang, Y.; Xu, X.; Liu, Y.; Chen, L. J.; Zhao, J. W. Construction of Ln^{3+}-substituted arsenotungstates modified by 2,5-thiophenedicarboxylic acid and application in selective fluorescence detection of Ba^{2+} in aqueous solution. *Inorg. Chem.* **2020**, *59*, 6839−6848.

(18) Li, Y. M.; Li, H. L.; Jiang, J.; Chen, L. J.; Zhao, J. W. Three types of distinguishing L-alanine-decorated and rare-earth-incorporated arsenotungstate hybrids prepared in a facile one-step assembly strategy. *Inorg. Chem.* **2019**, *58*, 3479−3491.

(19) Shang, S. X.; Lin, Z. G.; Yin, A. X.; Yang, S.; Chi, Y. N.; Wang, Y.; Dong, J.; Liu, B.; Zhen, N.; Hill, C. L.; Hu, C. W. Self-assembly of Ln(III)-containing tungstotellurates(VI): correlation of structure and photoluminescence. *Inorg. Chem.* **2018**, *57*, 8831−8840.

(20) Zhao, J. W.; Li, Y. Z.; Chen, L. J.; Yang, G. Y. Research progress on polyoxometalate-based transition-metal−rare-earth heterometallic derived materials: synthetic strategies, structural overview and functional applications. *Chem. Commun.* **2016**, *52*, 4418−4445.

(21) Zheng, Q.; Vilà-Nadal, L.; Lang, Z.; Chen, J. J.; Long, D. L.; Mathieson, J. S.; Poblet, J. M.; Cronin, L. Self-sorting of heteroanions in the assembly of cross-shaped polyoxometalate clusters. *J. Am. Chem. Soc.* **2018**, *140*, 2595−2601.

(22) Li, X. X.; Zhao, D.; Zheng, S. T. Recent advances in POM-organic frameworks and POM-organic polyhedra. *Coord. Chem. Rev.* **2019**, *397*, 220−240.

(23) Gao, J.; Yan, J.; Beeg, S.; Long, D. L.; Cronin, L. One-pot versus sequential reactions in the self-assembly of gigantic nanoscale polyoxotungstates. *J. Am. Chem. Soc.* **2013**, *135*, 1796−1805.

(24) Liu, L. L.; Jiang, J.; Liu, X. Y.; Liu, G. P.; Wang, D.; Chen, L. J.; Zhao, J. First series of mixed (P^{III}, Se^{IV})-heteroatoms oriented rare-earth embedded polyoxotungstates containing distinct building blocks. *Inorg. Chem. Front.* **2020**, *7*, 4640−4651.

(25) Liu, Y. W.; Liu, S. M.; Lai, X. Y.; Miao, J.; He, D. F.; Li, N.; Luo, F.; Shi, Z.; Liu, S. X. Polyoxometalate-modified sponge-like graphene oxide monolith with high proton-conducting performance. *Adv. Funct. Mater.* **2015**, *25*, 4480−4485.

(26) Liu, J. C.; Luo, j.; Han, Q.; Cao, J.; Chen, L. J.; Song, Y.; Zhao, J. W. Coexistence of long-range ferromagnetic ordering and spin-glass behavior observed in the first inorganic−organic hybrid 1-D oxalate-bridging nona-Mn^{II} sandwiched tungstoantimonate chain. *J. Mater. Chem. C* **2017**, *5*, 2043−2055.
(27) Goura, J.; Bassil, B. S.; Bindra, J. K.; Rutkowska, I. A.; Kulesza, P. J.; Dalal, N. S.; Kortz, U. Fe^{III}_{48}-Containing 96-tungsto-16-phosphate: synthesis, structure, magnetism and electrochemistry. *Chem. - Eur. J.* **2020**, *26*, 15821−15824.
(28) Wang, Y. J.; Wu, S. Y.; Sun, Y. Q.; Li, X. X.; Zheng, S. T. Octahedron-shaped three-shell Ln_{14}-substituted polyoxotungsto-germanates encapsulating a W_4O_{15} cluster: luminescence and frequency dependent magnetic properties. *Chem. Commun.* **2019**, *55*, 2857−2860.
(29) Ma, X.; Yang, W.; Chen, L. J.; Zhao, J. W. Significant developments on rare-earth-containing polyoxometalate chemistry: synthetic strategies, structural diversities and correlative properties. *CrystEngComm* **2015**, *17*, 8175−8197.
(30) Wassermann, K.; Dickman, M. H.; Pope, M. T. Self-assembly of supramolecular polyoxometalates: the compact, water-soluble heteropolytungstate anion $[As_{12}Ce_{16}(H_2O)_{36}W_{148}O_{524}]^{76-}$. *Angew. Chem., Int. Ed. Engl.* **1997**, *36*, 1445−1448.
(31) Yamase, T.; Naruke, H.; Sasaki, Y. Crystallographic characterization of the polyoxotungstate $[Eu_3(H_20)_3(SbW_90_{33})(W_50_{18})_3]^{18-}$and energy transfer in its crystalline lattices. *J. Chem. Soc., Dalton Trans.* **1990**, *5*, 1687−1696.
(32) Xue, G. L.; Vaissermann, J.; Gouzerh, P. Cerium(III) complexes with lacunary polyoxotungstates. synthesis and structural characterization of a novel heteropolyoxotungstate based on α-$[SbW_9O_{33}]^{9-}$ units. *J. Cluster Sci.* **2002**, *13*, 409−421.
(33) Zhao, J. W.; Cao, J.; Li, Y. Z.; Zhang, J.; Chen, L. J. First tungstoantimonate-based transition-metal−lanthanide heterometallic hybrids functionalized by aminoacid ligands. *Cryst. Growth Des.* **2014**, *14*, 6217−6229.
(34) Chen, L. J.; Cao, J.; Li, X. H.; Ma, X.; Luo, J.; Zhao, J. W. The first purely inorganic polyoxotungstates constructed from dimeric tungstoantimonate-based iron−rare-earth heterometallic fragments. *CrystEngComm* **2015**, *17*, 5002−5013.
(35) Artetxe, B.; Reinoso, S.; San Felices, L.; Lezama, L.; Gutiérrez-Zorrilla, J. M.; Vicent, S.; Haso, F.; Liu, T. B. New perspectives for old clusters: Anderson−Evans anions as building blocks of Large polyoxometalate frameworks in a series of heterometallic 3d−4f species. *Chem. - Eur. J.* **2016**, *22*, 4616−4625.
(36) Xu, X.; Chen, Y. H.; Zhang, Y.; Liu, Y. F.; Chen, L. J.; Zhao, J. W. Rare-earth and antimony-oxo clusters simultaneously connecting antimonotungstates comprising divacant and tetravacant keggin fragments. *Inorg. Chem.* **2019**, *58*, 11636−11648.
(37) Ibrahim, M.; Mal, S. S.; Bassil, B. S.; Banerjee, A.; Kortz, U. Yttrium(III)-containing tungstoantimonate(III) stabilized by tetrahedral WO_4^{2-} capping unit, $[\{Y(\alpha\text{-}SbW_9O_{31}(OH)_2)(CH_3COO)(H_2O)\}_3(WO_4)]^{17-}$. *Inorg. Chem.* **2011**, *50*, 956−960.
(38) Li, L. L.; Han, H. Y.; Wang, Y. H.; Tan, H. Q.; Zang, H. Y.; Li, Y. G. Construction of polyoxometalates from dynamic lacunary polyoxotungstate building blocks and lanthanide linkers. *Dalton. Trans.* **2015**, *44*, 11429−11436.
(39) Cai, J.; Zheng, X. Y.; Xie, J.; Yan, Z. H.; Kong, X. J.; Ren, Y. P.; Long, L. S.; Zheng, L. S. Anion dependent assembly of heterometallic 3d−4f clusters based on a lacunary polyoxometalate. *Inorg. Chem.* **2017**, *56*, 8439−8445.
(40) Tortajada, A.; Ninokata, R.; Martin, R. Ni-catalyzed site-selective dicarboxylation of 1,3-dienes with CO2. *J. Am. Chem. Soc.* **2018**, *140*, 2050−2053.
(41) Gaydou, M.; Moragas, T.; Julia-Hernandez, F.; Martin, R. Site-selective catalytic carboxylation of unsaturated hydrocarbons with CO2 and Water. *J. Am. Chem. Soc.* **2017**, *139*, 12161−12164.
(42) Ostapowicz, T. G.; Schmitz, M.; Krystof, M.; Klankermayer, J.; Leitner, W. Carbon dioxide as a C1 building block for the formation of carboxylic acids by formal catalytic hydrocarboxylation. *Angew. Chem., Int. Ed.* **2013**, *52*, 12119−12123.
(43) Wang, D.; Liu, L. L.; Jiang, J.; Chen, L. J.; Zhao, J. W. Polyoxometalate-based composite materials in electrochemistry: state-of-the-art progress and future outlook. *Nanoscale* **2020**, *12*, 5705−5718.
(44) Zhang, Y. T.; Gan, H. G.; Qin, C.; Wang, X. L.; Su, Z. M.; Zaworotko, M. J. Self-assembly of Goldberg polyhedra from a concave $[WV_5O_{11}(RCO_2)_5(SO_4)]^{3-}$ building block with 5-fold symmetry. *J. Am. Chem. Soc.* **2018**, *140*, 17365−17368.
(45) Yan, J.; Long, D. L.; Cronin, L. Development of a building block strategy to access gigantic nanoscale heteropolyoxotungstates by using SeO_3^{2-}as a template linker. *Angew. Chem., Int. Ed.* **2010**, *49*, 4117−4120.
(46) Fan, L. F.; Zhao, G. H.; Shi, H. J.; Liu, M. C.; Wang, Y. B.; Ke, H. Y. A femtomolar level and highly delective 17β-estradiol photoelectrochemical aptasensor applied in environmental water samples analysis. *Environ. Sci. Technol.* **2014**, *48*, 5754−5761.
(47) Yang, Y.; Li, M. X.; Zhu, Z. W. A novel electrochemical sensor based on carbon nanotubes array for selective detection of dopamine or uric acid. *Talanta* **2019**, *201*, 295−300.
(48) Sun, C. L.; Lee, H. H.; Yang, J. M.; Wu, C. C. The simultaneous electrochemical detection of ascorbic acid, dopamine, and uric acid using graphene/size-selected Pt nanocomposites. *Biosens. Bioelectron.* **2011**, *26*, 3450−3455.
(49) Zhang, W. J.; Liu, L.; Li, Y. G.; Wang, D. Y.; Ma, H.; Ren, H. L.; Shi, Y. L.; Han, Y. J.; Ye, B. C. Electrochemical sensing platform based on the biomass-derived microporous carbons for simultaneous determination of ascorbic acid, dopamine, and uric acid. *Biosens. Bioelectron.* **2018**, *121*, 96−103.
(50) Zhang, Y.; Jiang, J.; Liu, Y. F.; Li, P.; Liu, Y.; Chen, L. J.; Zhao, J. W. Multi-praseodymium-and-tungsten bridging octameric tellurotungstate and its 2D honeycomb composite film for detecting estrogen. *Nanoscale* **2020**, *12*, 10842−10853.
(51) Thakur, N.; Das Adhikary, S.; Kumar, M.; Mehta, D.; Padhan, A. K.; Mandal, D.; Nagaiah, T. C. Ultrasensitive and highly selective electrochemical detection of dopamine using poly(ionic liquids)−cobalt polyoxometalate/CNT composite. *ACS. Omega* **2018**, *3*, 2966−2973.
(52) Salavagione, H. J.; Díez-Pascual, A. M.; Lázaro, E.; Vera, S.; Gómez-Fatou, M. A. Chemical sensors based on polymer composites with carbon nanotubes and graphene: the role of the polymer. *J. Mater. Chem. A* **2014**, *2*, 14289−14328.
(53) Dolbecq, A.; Dumas, E.; Mayer, C. R.; Mialane, P. Hybrid organic-inorganic polyoxometalate compounds: from structural diversity to applications. *Chem. Rev.* **2010**, *110*, 6009−6048.
(54) Tsierkezos, N. G.; Ritter, U.; Thaha, Y. N.; Downing, C.; Szroeder, P.; Scharff, P. Multi-walled carbon nanotubes doped with boron as an electrode material for electrochemical studies on dopamine, uric acid, and ascorbic acid. *Microchim. Acta* **2016**, *183*, 35−47.
(55) Wang, J. L.; Munir, A.; Li, Z. H.; Zhou, S. S. Aptamer-Au NPs conjugates-accumulated methylene blue for the sensitive electrochemical immunoassay of protein. *Talanta* **2010**, *81*, 63−67.
(56) Zhao, G. F.; Zhou, X.; Ran, X.; Tan, X. P.; Li, T. H.; Cao, M.; Yang, L.; Du, G. B. Layer-by-layer assembly of anionic-/cationic-pillar[5]arenes multilayer films as chiral interface for electrochemical recognition of tryptophan isomers. *Electrochim. Acta* **2018**, *277*, 1−8.

https://doi.org/10.1021/acs.inorgchem.1c00890
Inorg. Chem. XXXX, XXX, XXX−XXX